21st Applied Aerodynamics Conference
23-26 June 2003, Orlando, Florida

AIAA 2003-4079

CFD Analysis for Ducted Fans with Validation

I-Chung Chang *
NASA Ames Research Center, Moffett Field, CA
R. G. Rajagopalan †
Iowa State University, Ames, IA

An axisymmetric, incompressible Navier-Stokes solver was developed to calculate the flow field of a ducted fan. The fan effect is modeled via the momentum source concept. The effects of the spinning fan blades were introduced into the flow field as time-averaged sources in the momentum equations. These source terms were not known *a priori* but are the result of the flow solution at each iteration. This approach simplified the modeling of the fan blades and provided a very rapid solution procedure for the flow problem.

A new grid generator capable of recognizing the duct and nacelle geometry was developed and tested for several industrial ducted fans of current interest. Prediction of hover performance for a ducted fan model was calculated and compared with available wind tunnel test data. The comparison was good. Preliminary results showed that the Computational Fluid Dynamics (CFD) program could be used as an axial flow analysis tool for ducted fan design.

Introduction

The concept of ducted fans as a suitable propulsive device for certain vertical/short take-off and landing (V/STOL) applications has been explored for more than a quarter century; the BELL X-22A is a good example of a successful application. In the 1970s, the ducted propeller was seen as a "quiet" propulsive device with the potential to meet the noise requirements of the 1980s and beyond. The 1990s saw the ducted fan as a viable concept for several unmanned air vehicles (UAV) such as Sikorsky's Cypher and Micro-Craft's Lift Augmented Ducted Fan (LADF). The UAVs have a small footprint and are light, making them efficient for vertical take-off and landing. The noise characteristics of the ducted fans also make them suitable for undetected surveillance.

The viscous flow through a ducted fan is very complex. The clearance between the tip of the fan blades and the duct is several orders of magnitude smaller than the fan radius. It strongly affects the characteristics of the flow through the ducted fan and consequently the performance of the ducted fan system. The inflow lip region is another geometric characteristic that influences the performance of the system. The shape of the duct, geometry of the nacelle and position of the fan within the duct all play important roles in the determination of the performance of the ducted fan. For analysis tools to be successful in ducted fan design, they must be capable of including as much of the detail of the geometry of the system as possible.

Simple momentum balance methods[1–3] assume uniform inflow and outflow with the direction of flow parallel to the duct axis. In addition, the fan is treated as an actuator disk with constant inflow. The results obtained with these ideal assumptions are essentially useful only for approximate comparison with experiments and for predicting the upper limit on the performance. In such simplified analysis the geometric characteristics of the duct, blades, hub and guiding vanes are not properly represented.

Some of the problems associated with the representation of the geometry and surfaces of the ducted fan were eliminated by potential flow methods.[4–6] However, the inherent assumptions of potential flow (inviscid, irrotational and incompressible) preclude estimation of important characteristics of the duct such as friction drag, location of the center of pressure, and stall characteristics of the duct. Also, due to the linear nature of the analysis, mutual interference effects between duct and fan are ignored. As a result, all basic design studies were made using costly wind tunnel experiments.

In the early 1960s, extensive wind tunnel experiments[7–10] were conducted and a wealth of data on the thrust, drag and efficiency of scale models and prototypes was collected. But, specific application was the guiding principle of the work, and parametric study proved costly. In the 1970s, Davis[11] reported on the work performed in the United Kingdom to validate the claim that the ducted propeller is a quiet and cost effective propulsive device. NASA also conducted several experimental studies[12–16] to investigate integrated performance of ducted propellers mounted on wings and full aircraft. These research efforts were very informative regarding the control characteristics of aircraft with ducted propellers. Nevertheless, most of the experimental research was designed for specific

*Senior AIAA member
†AIAA member

applications and not for the basic research of the flow through the ducted fan.

In the next section, the viscous flow analysis code for a ducted fan will be described.

Computational Procedure

The choice of the flow solver and the technique used for modeling the fan are central to the present CFD code. Their essential details are described here.

Flow Governing Equations

The flow around a ducted fan is mostly low-speed, except near the fan blade tips. The flow field is basically governed by the unsteady, laminar, incompressible Navier-Stokes equations. For incompressible flow, conservation of mass and momentum are sufficient conditions for defining the flow field. The conservation of mass applied to a fluid passing through an infinitesimal fixed control volume yields the equation of continuity:

$$\frac{\partial \rho}{\partial t} + \nabla \bullet \left(\rho \vec{V}\right) = 0 \tag{1}$$

Newton's second law applied to a fluid passing through the control volume yields the momentum equation:

$$\frac{\partial}{\partial t}\left(\rho \vec{V}\right) + \nabla \bullet \rho \vec{V}\vec{V} = \rho \vec{f} + \nabla \bullet \Pi_{ij} + S' \tag{2}$$

For an axisymmetric system, the flow equations in scalar form are as follows:

Continuity equation:

$$\frac{1}{r}\left[\frac{\partial}{\partial r}\left(r\ \rho V_r\right) + \frac{\partial}{\partial z}\left(r\ \rho V_z\right)\right] = 0 \tag{3}$$

r momentum equation:

$$\frac{\partial}{\partial t}\left(\rho V_r\right) + \frac{1}{r}\left[\frac{\partial}{\partial r}\left(r\ \rho {V_r}^2 - \mu r \frac{\partial V_r}{\partial r}\right) + \frac{\partial}{\partial z}\left(r\ \rho V_z V_r - \mu r \frac{\partial V_r}{\partial z}\right)\right] = -\frac{\partial p}{\partial r} + \frac{\rho {V_\theta}^2}{r} - \frac{\mu V_r}{r^2} + S'_r \tag{4}$$

θ momentum equation:

$$\frac{\partial}{\partial t}\left(\rho V_\theta\right) + \frac{1}{r}\left[\frac{\partial}{\partial r}\left(r\ \rho V_r V_\theta - \mu r \frac{\partial V_\theta}{\partial r}\right) + \frac{\partial}{\partial z}\left(r\ \rho V_z V_\theta - \mu r \frac{\partial V_\theta}{\partial z}\right)\right] = -\frac{\rho V_r V_\theta}{r} - \frac{\mu V_\theta}{r^2} + S'_\theta \tag{5}$$

z momentum equation:

$$\frac{\partial}{\partial t}\left(\rho V_z\right) + \frac{1}{r}\left[\frac{\partial}{\partial r}\left(r\ \rho V_r V_z - \mu r \frac{\partial V_z}{\partial r}\right) + \frac{\partial}{\partial z}\left(r\ \rho {V_z}^2 - \mu r \frac{\partial V_z}{\partial z}\right)\right] = -\frac{\partial p}{\partial z} + S'_z \tag{6}$$

where S'_r, S'_θ and S'_z are source terms through which the influence of the fan is introduced into the surrounding flow field.

Discretization of the Flow Governing Equations

Consider the following generic governing equation for an axisymmetric system:

$$\frac{\partial}{\partial t}\left(\rho T\right) + \frac{1}{r}\left[\frac{\partial}{\partial r}\left(r\ \rho V_r\ T - \mu r \frac{\partial T}{\partial r}\right) + \frac{\partial}{\partial z}\left(r\ \rho V_z\ T - \mu r \frac{\partial T}{\partial z}\right)\right] = s \tag{7}$$

where s represents the terms on the right side of the momentum equations, excluding the fan sources.

Defining the following total fluxes,

$$\begin{aligned} J_r &= \left(r\ \rho V_r\ T - \mu r \frac{\partial T}{\partial r}\right) \\ J_z &= \left(r\ \rho V_z\ T - \mu r \frac{\partial T}{\partial z}\right) \end{aligned}$$

Equation 7 can be rewritten as

$$\frac{\partial}{\partial t}\left(\rho T\right) + \frac{1}{r}\left[\frac{\partial}{\partial r}\left(J_r\right) + \frac{\partial}{\partial z}\left(J_z\right)\right] = s \tag{8}$$

Integrating the above equation over the control volume shown in Figure 1 yields:

$$\int_w^e \int_b^t \int_s^n \int_{t_o}^{t_1} \frac{\partial}{\partial t}\left(\rho T\right)\ \ r\ dt\ dr\ d\theta\ dz +$$

$$\int_{t_o}^{t_1} \int_w^e \int_b^t \int_s^n \frac{1}{r}\frac{\partial}{\partial r}\left(J_r\right)\ \ r\ dr\ d\theta\ dz\ dt +$$

$$\int_{t_o}^{t_1} \int_w^e \int_b^t \int_s^n \frac{1}{r}\frac{\partial}{\partial \theta}\left(J_\theta\right)\ \ r\ dr\ d\theta\ dz\ dt +$$

$$\int_{t_o}^{t_1} \int_w^e \int_b^t \int_s^n \frac{1}{r}\frac{\partial}{\partial z}\left(J_z\right)\ \ r\ dr\ d\theta\ dz\ dt$$

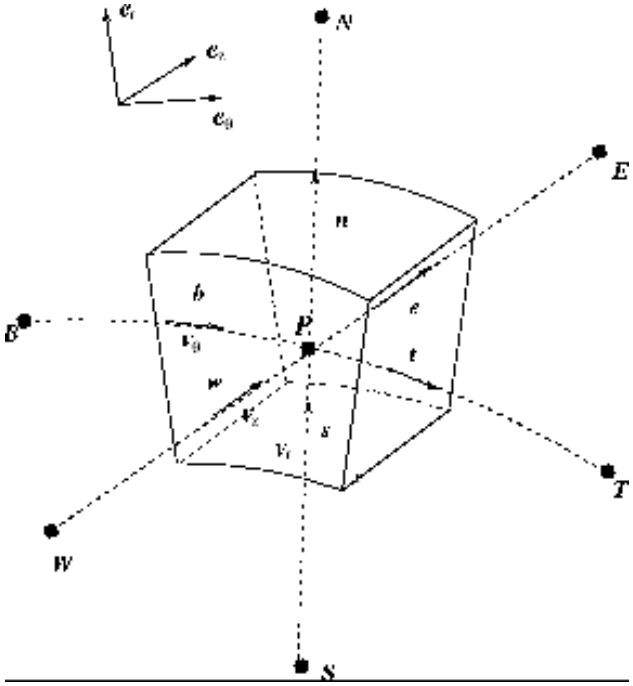

Fig. 1 A typical control volume in an axisymmetric grid

$$= \int_{t_o}^{t_1} \int_{w}^{e} \int_{b}^{t} \int_{s}^{n} s \;\; r \; dr \; d\theta \; dz \; dt \tag{9}$$

The integration over the time interval can be generalized by the following assumptions:

$$\int_{t_o}^{t_1} T_P \; dt = \left[f {T_P}^1 + (1-f) {T_P}^o \right] \Delta t \tag{10}$$

where f is a weighting factor between 0 and 1; superscript 1 indicates the new values of the corresponding variables at t=t_1 seconds; superscript o refers to old values of the variables at t_o.

Using the assumption in Equation 10, the integration of Equation 9 divided by Δt yields the following:

$$\frac{\left[(\rho T)^1 - (\rho T)^o \right]}{\Delta t} \;\; r_j \Delta r \; \Delta\theta \; \Delta z + f \; [J_n - J_s]^1 +$$

$$(1-f) \; [J_n - J_s]^o + f \; [J_e - J_w]^1 + (1-f) \; [J_e - J_w]^o$$

$$= f \; [(s_{const} + s_{coef} T_P) \;\; r_j \; \Delta r \; \Delta\theta \; \Delta z]^1 +$$

$$(1-f) \; [(s_{const} + s_{coef} T_P) \;\; r_j \; \Delta r \; \Delta\theta \; \Delta z]^o \tag{11}$$

where $(s_{const} + s_{coef} T_P)$ is the linearized source term. The term, s_{const}, is the constant part of the linearized source term and s_{coef}, is the coefficient of the independent variable T evaluated at the point P. The integrated total fluxes over the control volume faces J_n, J_s, J_e, J_w are given by:

$$\begin{aligned} J_n &= (J_r)_n \;\; (r \; \Delta\theta \; \Delta z)_n \\ J_s &= (J_r)_s \;\; (r \; \Delta\theta \; \Delta z)_s \\ J_e &= (J_z)_e \;\; (r \; \Delta r \; \Delta\theta)_e \\ J_w &= (J_z)_w \;\; (r \; \Delta r \; \Delta\theta)_w \end{aligned}$$

In a similar fashion the continuity equation (Equation 3) can be integrated over the control volume:

$$\int_{t_o}^{t_1} \int_{w}^{e} \int_{b}^{t} \int_{s}^{n} \frac{1}{r} \frac{\partial}{\partial r} (r \rho V_r) \;\; r \; dr \; d\theta \; dz \; dt +$$

$$\int_{t_o}^{t_1} \int_{s}^{n} \int_{b}^{t} \int_{w}^{e} \frac{1}{r} \frac{\partial}{\partial z} (r \rho V_z) \;\; r \; dz \; d\theta \; dr \; dt = 0$$

The integration yields:

$$\begin{aligned} &f \; (F_n - F_s)^1 + (1-f) \; (F_n - F_s)^o + \\ &f \; (F_e - F_w)^1 + (1-f) \; (F_e - F_w)^o = 0 \end{aligned} \tag{12}$$

where the total mass fluxes F_n, F_s, F_t, F_b, F_e and F_w are given by:

$$\begin{aligned} F_n &= (\rho V_r)_n (r \; \Delta\theta \; \Delta z)_n \\ F_s &= (\rho V_r)_s (r \; \Delta\theta \; \Delta z)_s \\ F_e &= (\rho V_z)_e (r \; \Delta\theta \; \Delta r)_e \\ F_w &= (\rho V_z)_w (r \; \Delta\theta \; \Delta r)_w \end{aligned}$$

Multiplying Equation 12 by T_P and subtracting it from Equation 11 results in the following equation:

$$\begin{aligned} &\frac{\left[(\rho T)^1 - (\rho T)^o \right]}{\Delta t} \;\; r_P \Delta r \; \Delta\theta \; \Delta z + \\ &f \; [J_n - F_n \; T_P]^1 + (1-f) \; [J_n - F_n \; T_P]^o + \\ &f \; [J_s - F_s \; T_P]^1 + (1-f) \; [J_s - F_s \; T_P]^o + \\ &f \; (J_e - F_e \; T_P)^1 + (1-f) \; (J_e - F_e \; T_P)^o + \\ &f \; (J_w - F_w \; T_P)^1 + (1-f) \; (J_w - F_w \; T_P)^o + \\ &(1-f) \; [J_n - F_n \; T_P]^1 + (1-f) \; [J_n - F_n \; T_P]^o + \\ &(1-f) \; [J_s - F_s \; T_P]^1 + (1-f) \; [J_s - F_s \; T_P]^o + \\ &(1-f) \; (J_e - F_e \; T_P)^1 + (1-f) \; (J_e - F_e \; T_P)^o + \\ &(1-f) \; (J_w - F_w \; T_P)^1 + (1-f) \; (J_w - F_w \; T_P)^o + \\ &= f \; [(s_{const} + s_{coef} T_P) \;\; r_P \; \Delta r \; \Delta\theta \; \Delta z]^1 + \\ &(1-f) [(s_{const} + s_{coef} T_P) \;\; r_P \; \Delta r \; \Delta\theta \; \Delta z]^o \end{aligned} \tag{13}$$

Following the procedure explained in Chapter 5 of Reference,[17] the terms between the brackets in Equa-

tion 13 can be replaced by:

$$\begin{aligned}(J_n - F_n\ T_P) &= A_N\,(T_P - T_N)\\ (J_s - F_s\ T_P) &= A_S\,(T_S - T_P)\\ (J_e - F_e\ T_P) &= A_E\,(T_P - T_E)\\ (J_w - F_w\ T_P) &= A_W\,(T_W - T_P)\end{aligned}$$

For convenience, the superscript for new values is dropped. Consequently, the final discretized generic equation can be written as:

$$\begin{aligned}a_P T_P &= a_E T_E + a_W T_W + a_N T_N + a_S T_S + \\ &\quad a_T T_T + a_B T_B + b \\ &= \sum a_{nb} T_{nb} + b \end{aligned} \tag{14}$$

where E, W, N and S refer to east, west, north, and south grid points respectively; nb refers to the points neighboring the point P. The coefficients a_E, a_W, a_N and a_S contain the convection and diffusion terms and are given by the following relations:

$$\begin{aligned}a_E &= D_e A\,(|P_e|) + [\![-F_e, 0]\!]\\ a_W &= D_w A\,(|P_w|) + [\![F_w, 0]\!]\\ a_N &= D_n A\,(|P_n|) + [\![-F_n, 0]\!]\\ a_S &= D_s A\,(|P_s|) + [\![F_s, 0]\!]\\ a_P &= f\ (a_E + a_W + a_N + a_S) + \\ &\quad \frac{\rho\ r_P \Delta r\ \Delta\theta\ \Delta z}{\Delta t} - f\ s_{coef}\ \Delta V\\ b &= f\ s_{const}\ \Delta V + (1-f)\ {s_{const}}^o\ \Delta V + \\ &\quad (1-f)\ \sum {a_{nb}}^o {T_{nb}}^o + \\ &\quad \frac{\rho\ r_P \Delta r\ \Delta\theta\ \Delta z}{\Delta t} {T_P}^o\end{aligned} \tag{15}$$

where P_e, P_w, P_n and P_s are the Peclet numbers, which are the ratio of F (the flow rate across the surface of the control volume) and D (the diffusion across the surface of the control volume). The symbol $[\![\ ]\!]$ denotes the greater of the quantities within.

The power-law scheme was selected for the function $A\,(|P|)$, which is given by

$$A\,(|P|) = [\![0, (1 - 0.1\,|P|)^5]\!] \tag{16}$$

The above function is a curve fit of the exact solution of the steady one-dimensional convection/diffusion problem of the general dependent variable T. The variation of T is dependent on the convection (F) and diffusion (D) given by:

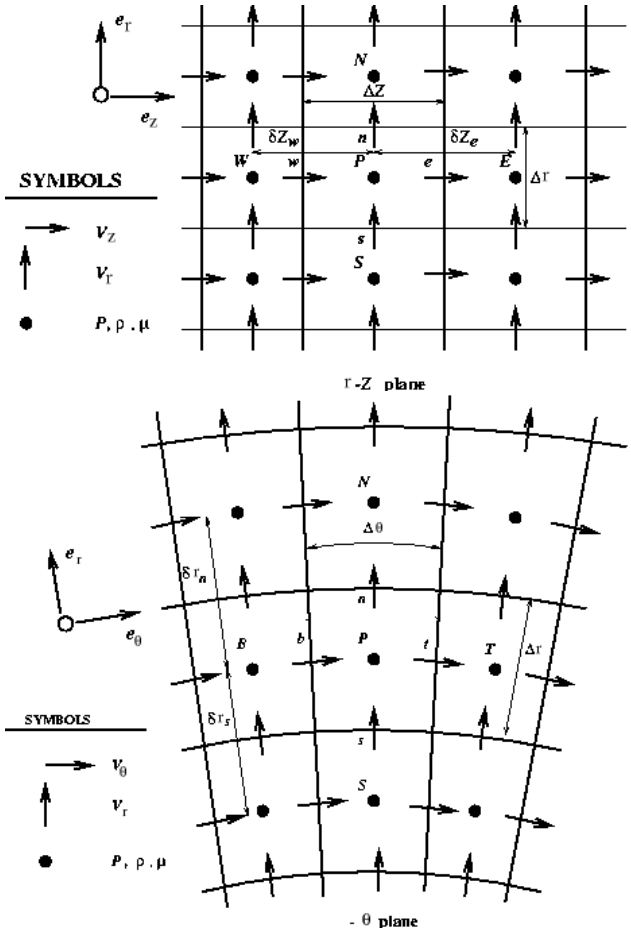

Fig. 2 The staggered grid

$$\begin{aligned}F_e &= (\rho V_z)_e\,(r\ \Delta\theta\ \Delta r)_e\\ D_e &= \frac{\mu_e}{\delta z_e}\,(r\ \Delta\theta\ \Delta r)_e\\ F_w &= (\rho V_z)_w\,(r\ \Delta\theta\ \Delta r)_w\\ D_w &= \frac{\mu_w}{\delta z_w}\,(r\ \Delta\theta\ \Delta r)_w\\ F_n &= (\rho V_r)_n\,(r\ \Delta\theta\ \Delta z)_n\\ D_n &= \frac{\mu_n}{\delta r_n}\,(r\ \Delta\theta\ \Delta z)_n\\ F_s &= (\rho V_r)_s\,(r\ \Delta\theta\ \Delta z)_s\\ D_s &= \frac{\mu_s}{\delta r_s}\,(r\ \Delta\theta\ \Delta z)_s\end{aligned} \tag{17}$$

where the suffixes e, w, n and s refer to control volume faces; δr, δz are the distances between grid points as illustrated in Figure 2. The value of diffusion pertaining to control volume faces is determined through the use of harmonic mean.

Until now, all the integrations were applied to the general control volume in Figure 1. It is important to note that the grid used for solving the momentum equations is staggered. In other words, the control volume is different for each of the momentum equations.

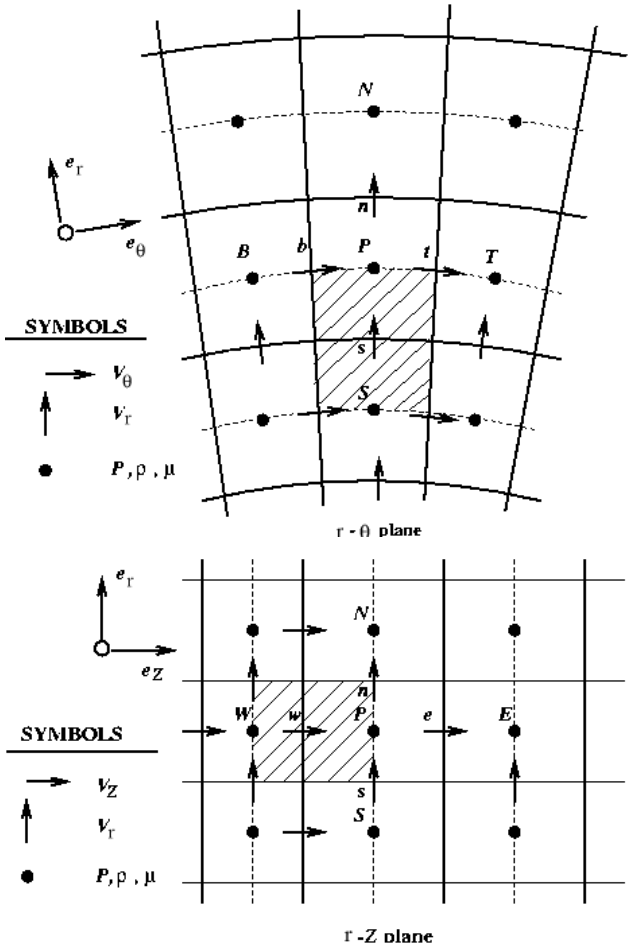

Fig. 3 a. V_r grid cell b. V_z grid cell

Therefore, a shift in indexing needs to be applied to the discretized equations. The staggered grid for the momentum equations is shown in Figure 3.

In addition, by taking advantage of an axisymmetric system, only one control volume in the θ-direction is used. For convenience, the term $\Delta\theta$ is taken to be 1.0 radian.

Discretization of the Momentum Equation Source Terms

The aim in this section is to integrate, discretize and linearize the right-hand side of the momentum equations (4-6). The integration process first takes place on a control volume similar to the one in Figure 1; however, here we abandon the E, W, N, S, grid point referencing and instead use the classical i, j referencing (see Figure 4). Since each of the three momentum equations are solved on a different staggered grid, a shift in indexing is applied on the discretized source terms to properly match the corresponding staggered grid. The integration in the θ-direction will be taken from 0. to 1. radian.

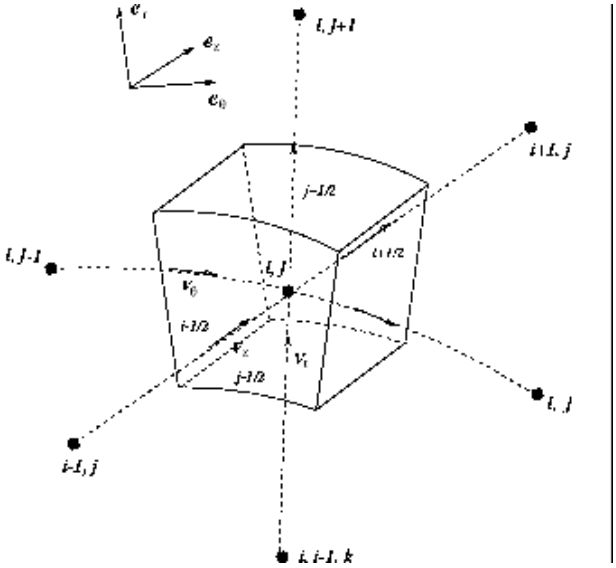

Fig. 4 Control volume numbering

The source terms of Equations 4-6 are given by:

$$
\begin{aligned}
r-momentum\ source\ terms &= -\frac{\partial p}{\partial r}+\frac{\rho {V_\theta}^2}{r} \\
&\quad -\frac{\mu V_r}{r^2} \\
\theta-momentum\ source\ terms &= -\frac{\rho V_r V_\theta}{r}-\frac{\mu V_\theta}{r^2} \\
z-momentum\ source\ terms &= -\frac{\partial p}{\partial z}
\end{aligned}
$$

Integration of the r-momentum Equation Source Terms

The source terms of the r-momentum equation must be discretized on the V_r-staggered grid. Therefore, the source terms are first integrated on the control volume shown in Figure 4, and then shifted by one-half control volume in the negative r-direction.

1. $\left(-\frac{\partial p}{\partial r}\right)$ term.

   The integration of $\left(-\frac{\partial p}{\partial r}\right)$ on a control volume yields:

$$
\begin{aligned}
&-\int_{i-\frac{1}{2}}^{i+\frac{1}{2}}\int_{0}^{1}\int_{j-\frac{1}{2}}^{j+\frac{1}{2}}\frac{\partial p}{\partial r}\ r\ dr\ d\theta\ dz \\
&=-\int_{i-\frac{1}{2}}^{i+\frac{1}{2}}\int_{0}^{1}\int_{j-\frac{1}{2}}^{j+\frac{1}{2}}\frac{\partial (p\ r)}{\partial r}\ dr\ d\theta\ dz \\
&\quad+\int_{i-\frac{1}{2}}^{i+\frac{1}{2}}\int_{0}^{1}\int_{j-\frac{1}{2}}^{j+\frac{1}{2}}p\ dr\ d\theta\ dz \\
&=-\left[(p\ r)_{j+\frac{1}{2}}-(p\ r)_{j-\frac{1}{2}}\right]\ \Delta z_i+\tilde{p}\ \Delta r_j\ \Delta z_i
\end{aligned}
$$

   Approximating:

$\tilde{p}$ by $\left(\frac{p_{j+\frac{1}{2}}+p_{j-\frac{1}{2}}}{2}\right)$

$r_{j+\frac{1}{2}}$ by $\left(r_j+\frac{\Delta r_j}{2}\right)$

$r_{j-\frac{1}{2}}$ by $\left(r_j-\frac{\Delta r_j}{2}\right)$

gives :

$$= -\left[p_{j+\frac{1}{2}}\left(r_j+\frac{\Delta r_j}{2}\right)-p_{j-\frac{1}{2}}\left(r_j-\frac{\Delta r_j}{2}\right)\right]\ \Delta zi + \left(p_{j+\frac{1}{2}}+p_{j-\frac{1}{2}}\right)\ \left(\frac{\Delta r_j}{2}\right)\ \Delta z_i$$
$$= \left(p_{j-\frac{1}{2}}-p_{j+\frac{1}{2}}\right)\ r_j\ \Delta z_i$$

For the V_r-staggered grid we shift the indexing by one-half control volume in the negative r-direction, to get:

$$= (p_{j-1}-p_j)\ \left(r_j-\frac{\Delta r_j}{2}\right)\ \Delta z_i$$

This term will be referred to as $(p_P - p_N)A_n$ in later sections.

2. $\left(\frac{\rho {V_\theta}^2}{r}\right)$ term.
Integrate $\left(\frac{\rho {V_\theta}^2}{r}\right)$ over the control volume to get:
$$\int_{i-\frac{1}{2}}^{i+\frac{1}{2}}\int_{0}^{1}\int_{j-\frac{1}{2}}^{j+\frac{1}{2}}\frac{\rho {V_\theta}^2}{r}\ r\ dr\ d\theta\ dz = \left(\rho {V_\theta}^2\right)_{i,j}\ \Delta r_j\ \Delta z_i$$
A shift of a one-half control volume in the negative r-direction yields
$$= \left(\rho {V_\theta}^2\right)_{i,j-\frac{1}{2}}\ (r_j - r_{j-1})\ \Delta z_i$$
The term obtained above is independent of the velocity V_r. Therefore, it is included into the constant part of the linearized source term, s_{const}.

3. $-\frac{\mu V_r}{r^2}$ term.
Again we integrate over the control volume to obtain:
$$-\int_{i-\frac{1}{2}}^{i+\frac{1}{2}}\int_{0}^{1}\int_{j-\frac{1}{2}}^{j+\frac{1}{2}}\frac{\mu V_r}{r^2}\ r\ dr\ d\theta\ dz = -\left(\mu V_r\right)_{i,j}\ln\left[\frac{r_{j+\frac{1}{2}}}{r_{j-\frac{1}{2}}}\right]\Delta z_i$$
and then we shift by one-half control volume in the negative r-direction to get
$$= -\left(\mu\right)_{i,j-\frac{1}{2}}\ V_{R_{i,j}}\ \ln\left[\frac{r_j}{r_{j-1}}\right]\Delta z_i$$[1]

[1]The reason the index $j-\frac{1}{2}$ is given to μ while the index j is given to V_r is: V_r is defined at the face of the control volume,(staggered grid), on the other hand μ is defined at the grid points. Therefore, the value of μ must be interpolated at $j-\frac{1}{2}$.

This source term is dependent on the V_r velocity. Therefore, the proper formulation is to include it into the s_{coef} part of the linearized source term.

Integration of the θ-momentum Equation Source Terms

Here, the source terms of the θ-momentum is integrated on the control volume shown in Figure 4, and then shifted by one-half control volume in the negative θ-direction to match the θ-staggered grid.

1. $-\frac{\rho V_r V_\theta}{r}$ term.
Integrate over the control volume to obtain:
$$-\int_{i-\frac{1}{2}}^{i+\frac{1}{2}}\int_{0}^{1}\int_{j-\frac{1}{2}}^{j+\frac{1}{2}}\frac{\rho V_r V_\theta}{r}\ r\ dr\ d\theta\ dz = -\left(\rho V_r V_\theta\right)_{i,j}\ \Delta r_j\ \Delta z_i$$
shift by one-half control volume in the negative θ-direction to get:
$$= -\left(\rho V_r\right)_{i,j-\frac{1}{2}}\ \left(V_\theta\right)_{i,j}\ \Delta r_j\ \Delta z_i$$
To satisfy the positive coefficient rule, that is s_{coef} must be positive, the linearization of this source term is as follows:
$$s_{const} = [\![-\left(\rho V_r\right)_{i,j-\frac{1}{2}}\ \Delta r_j\ \Delta z_i, 0]\!]\ \left(V_\theta\right)_{i,j}$$
$$s_{coef} = -[\![\left(\rho V_r\right)_{i,j-\frac{1}{2}}\ \Delta r_j\ \Delta z_i, 0]\!]$$

If V_r happens to be negative then the term s_{const} will be included in the constant source term. On the other hand, if V_r is positive, then the term s_{coef} will be included in the dependent source term.

2. $-\frac{\mu V_\theta}{r^2}$ term.
Integrate over the control volume to obtain:
$$-\int_{i-\frac{1}{2}}^{i+\frac{1}{2}}\int_{0}^{1}\int_{j-\frac{1}{2}}^{j+\frac{1}{2}}\frac{\mu V_\theta}{r^2}\ r\ dr\ d\theta\ dz = -\left(\mu V_\theta\right)_{i,j}\ \ln\left[\frac{r_{j+\frac{1}{2}}}{r_{j-\frac{1}{2}}}\right]\Delta z_i$$

Integration of the z-momentum Equation Source Terms

1. $-\frac{\partial p}{\partial z}$ term.
Integrate
$$-\int_{i-\frac{1}{2}}^{i+\frac{1}{2}}\int_{0}^{1}\int_{j-\frac{1}{2}}^{j+\frac{1}{2}}\frac{\partial p}{\partial z}\ r\ dr\ d\theta\ dz = -\int_{0}^{1}\int_{j-\frac{1}{2}}^{j+\frac{1}{2}} r\ \left(p_{i+\frac{1}{2},j}-p_{i-\frac{1}{2},j}\right)\ dr\ d\theta$$
$$= \left(p_{i-\frac{1}{2},j}-p_{i+\frac{1}{2},j}\right)\left(\frac{\left(r_{j+\frac{1}{2}}\right)^2-\left(r_{j-\frac{1}{2}}\right)^2}{2}\right)$$

$$= \left(p_{i-\frac{1}{2},j} - p_{i+\frac{1}{2},j}\right)\left(r_{j+\frac{1}{2}} - r_{j-\frac{1}{2}}\right)\left(\frac{r_{j+\frac{1}{2}} + r_{j-\frac{1}{2}}}{2}\right)$$

$$= \left(p_{i-\frac{1}{2},j} - p_{i+\frac{1}{2},j}\right)\ r_j\ \Delta r_j$$

shift by one-half control volume in the negative z-direction, to get:

$$= (p_{i-1,j} - p_{i,j})\ r_j\ \Delta r_j$$

Rotor Modeling

The fan modeling is based on the momentum source concept developed by Rajagopalan.[18–20] In order to obtain the wake of the fan, not known *a priori*, the action of the rotating blades has to be implicitly introduced into the governing equations. In other words, the effect of the spinning blades is in the form of the force **F**(x,y,z,t) imparted by the blade to the fluid particles in the path of the fan. Realizing that the momentum equation governs the balance of the rate of change of momentum and the external forces experienced by the fluid element, the effects of the spinning blade on its path at a given time can be modeled by including the force **F** (imparted by that fan at that particular time) to the momentum source at the cells occupied by the fan at that particular time. The force **F**(x,y,z,t) can be described by its components in each of the coordinate directions. These components of **F**(x,y,z,t) are introduced in the scalar momentum equations as implicit sources.

The force **-F** exerted by the fluid on the blade varies along the span of the blade and in general, may vary as a function of time as well. These variations are largely due to the local flow conditions, variations in the blade's chord, aerodynamic twist, and geometric twist along the span. As a result, the different segments of the blade will also see different strengths and directions of the relative wind, and the flow field around the fan itself may be inherently unsteady due to the presence of bodies. For a time-accurate calculation, the source terms in functional notation can be written as:

$$S_i = S_i(C_l, C_d, \alpha, \dot{\alpha}, v_{abs}, \omega, \mathbf{R}, t, c, \rho, \mu_{eff}, Re, M) \tag{18}$$

where C_l and C_d are airfoil characteristics of the fan blade, α is the angle of attack made by the fan blade to the relative velocity vector, $\dot{\alpha}$ is the time rate of change of α as the blade moves through a revolution, v_{abs} is the absolute velocity of the fluid at the instantaneous blade location $(\mathbf{R}, t)$, ω is the angular velocity of the fan, and c is the chord of the blade. Even though the complete Navier-Stokes equations are solved everywhere in the flow field, the dependence of S_i on μ and Re are considered only implicitly through the airfoil sectional characteristics C_l and C_d in this analysis.

Using this method it is necessary to divide the blade into many spanwise blade elements, where the blade properties (aerodynamic and geometric) are assumed to be constant for each element. Using velocities from the previous time-step, the relative wind for each blade element can be computed and then used to determine the lift and drag (using a look up table for the C_L and C_D) at each of the blade elements. The forces are resolved into the coordinate directions and included as sources in the corresponding momentum equations for the next solver iteration.

Since the blade does not occupy a given cell at all times as it sweeps the disk, only a fraction of the fan source needs to be allocated to that particular cell. This fraction is determined as follows.

The time taken by the center of the blade element to traverse one revolution is:

$$t_{1.rev} = \frac{2\pi}{\omega}\ , \tag{19}$$

where ω is the angular speed of the blade in radians/sec. The time the center of a blade element spends in a given cell is:

$$t_{\Delta\theta} = \frac{\Delta\theta}{\omega} \tag{20}$$

where $\Delta\theta$ is the angular measure of the path traced by a blade element as it passed through that cell. Therefore, the fractional time that the blade element spends in a cell is:

$$\begin{aligned} t_{frac} &= \frac{\Delta\theta/\omega}{2\pi/\omega} \\ &= \frac{\Delta\theta}{2\pi}\ , \end{aligned} \tag{21}$$

For a fan with N blades, this fraction becomes:

$$t_{frac} = N\frac{\Delta\theta}{2\pi}\ . \tag{22}$$

This time-averaging technique represents a convenient and reasonable approximation in the fan modeling procedure. While it is true that the flow through a fan is unsteady in nature, the flow in the immediate vicinity of the fan disk is mostly in the direction normal to the disk (except at the fan tip region), coupled with a strong swirling motion due to the shear imparted by the rotating blade. Since the mean of the flow quantities is large, the unsteady components can be averaged without compromising the physics of the solution. This time-averaged technique allows sufficiently large time steps to be taken to advance the solution, without constraint from the rotational speed of the blade, since no attempt is made to consider the specific blade locations at different times.

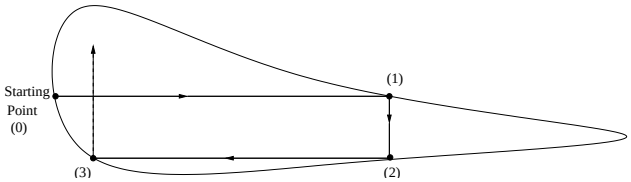

Fig. 5 The curve adaptive procedure used in grid generation.

Cartesian Grid Generation

The shape of the duct plays a very important role in the performance of a ducted propeller system. Therefore, proper representation of the duct geometry is critical. For maximum accuracy in the Cartesian coordinate system, the grids around the duct need to be arranged such that the boundaries of the duct pass through opposite corners of the surface cells. For this purpose, an option was added to the grid generation program to enforce the above criteria, known as "the curve adaptive option".

The following methodology is used to implement the curve adaptive option: First, an initial grid based on a user specified number of points on the body and cluster ratio is constructed. Then, from each specified point, the grid generator finds the next grid point on the body surface by moving in x or y directions. This procedure stops when: (1) two neighbor points are within a given tolerance, (2) the slope angle of the surface at the point is 0 or 90 degrees or (3) exceeding a preset number of movements. This procedure is depicted in Figure 5. Figure 6 shows the grids near a duct generated using the above procedure. As shown in the figure, the points on the boundary pass the cells diagonally.

Using the curve adaptive methodology, the resolution of the grid in the convex areas of the body surfaces is higher than other regions. In other words, this method may generate cells with high clustering ratio, which may result in numerical instabilities and grid shocks. To avoid these problems, a smoothing process is implemented into the grid generation program which ensures that the ratio between two adjacent grid cell sizes is no greater than 2.0. In this process, the grids around the duct may be changed slightly. The duct boundary does not cross the opposite corners of a few cells. An example of the final grid generated around the duct surface is shown in Figure 7.

Solution Procedure of the Discretized Equations

In this research, the discretized equations are solved using a finite-volume approach called SIMPLER, developed by Patankar.[17] This approach uses an iterative procedure to solve for the primitive variables (velocity and pressure fields). The discretized equations are solved using a line-by-line method combining the Tri-Diagonal Matrix Algorithm (TDMA) and the

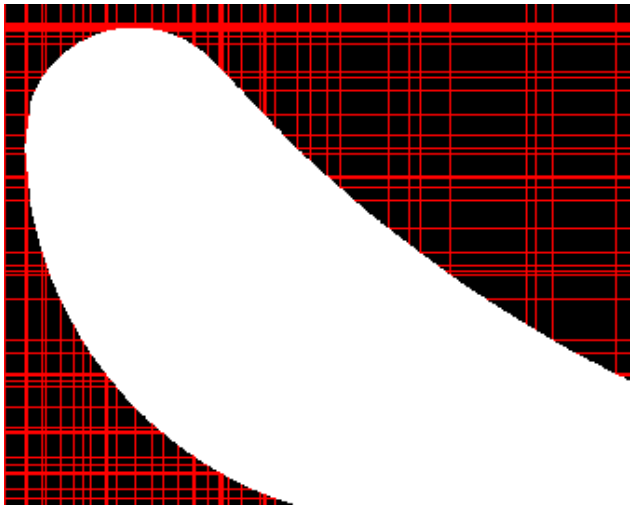

Fig. 6 A sample grid around a duct generated using curve adaptive option.

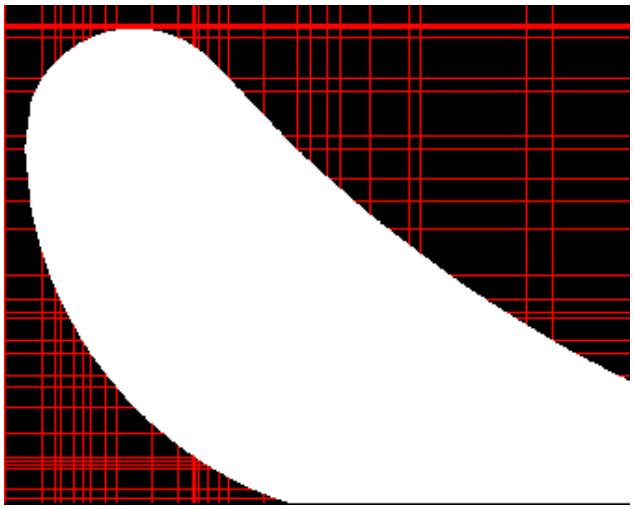

Fig. 7 A sample grid around the duct after smoothing process.

Gauss-Seidel method. The details of the SIMPLER algorithm can be found in Reference;[17] only highlights and important principles are presented here. A brief description of the momentum and pressure equations used in the SIMPLER algorithm follows.

Momentum Equations

By employing the formulation for discretizing the general differential equation, the discretized r–momentum equation on a staggered grid shown in Figure 3.a can be written as:

$$a_n V_{rn} = \sum a_{nb} V_{rnb} + b_r + (p_P - p_N) A_n \qquad (23)$$

where the neighboring coefficients a_{nb} account for the combined convection–diffusion influence at the control volume faces, b_r represents the discretized source term, the term $p_P - p_N$ is the pressure gradient acting on the control volume, and A_n is the area on which the pressure acts. The coefficients of the momentum equation

(a_e, a_w, a_n, a_s), being functions of the velocity components, make the momentum equation non-linear. This non-linearity is handled by adopting an iterative strategy and by lagging the coefficients.

Similarly, the θ–momentum equation and the z–momentum equation can also be discretized to yield the following:

$$a_t V_{\theta t} = \sum a_{nb} V_{\theta nb} + b_\theta \tag{24}$$

$$a_e V_{ze} = \sum a_{nb} V_{znb} + b_z + (p_P - p_E) A_e \tag{25}$$

The discretized momentum equations can be solved iteratively if the pressure field is known. If the correct pressure field is employed the resulting velocity field will satisfy the continuity equation. However, the pressure field is unknown and an equation for pressure must be derived to solve for it.

Pressure Equation and Pressure Correction Equation

Since the main driving force for the velocity from one cell to the next cell is the pressure difference between the two cells, an accurate solution of the pressure field is important. By manipulating the continuity equation and the momentum equation, an equation for pressure is derived and discretized to yield a form similar to Equation 14:[17]

$$a_P p_P = a_E p_E + a_W p_W + a_N p_N + a_S p_S + bp \tag{26}$$

If the correct velocity field is used in the above equation the correct pressure field will result. For a guessed velocity field, a pressure correction equation is required to correct the velocity field obtained from solving the momentum equation. Once more, the pressure correction equation is derived by manipulating the continuity and the momentum equations, and it is cast in a form similar to Equation 14. The purpose of the pressure correction equation is to improve the pressure field such that the velocity field will be corrected every iteration and progressively get closer to satisfying the continuity equation.

SIMPLER Algorithm

The sequence of steps for the unsteady SIMPLER algorithm can be summarized as follows:

1. Start with a given (guessed) velocity field.
2. Calculate the coefficients of the momentum and pressure equations.
3. Solve pressure equations to obtain the pressure field.
4. Using the calculated pressure field, solve the momentum equations to get the velocity field.
5. Calculate the source terms of the pressure correction equation and solve for the pressure corrections.
6. Correct the velocities using the velocity correction equations.
7. Return to step 2 and repeat until convergence.
8. Start with the next time.

Boundary Conditions

The velocities are set to freestream values at the inflow boundaries. The downstream boundary values are extrapolated from the interior grid points and adjusted to conserve mass flow through the computational domain. All the control volumes that lie in the solid region are blocked off with zero velocities everywhere. In other words, no-slip viscous boundary conditions are applied to all solid bodies.

Results

The Navier-Stokes flow code described earlier was applied to simulate the following two configurations:

- Trek Aeropspace's ducted fan
- Micro-Craft's Lift Augmented Ducted Fan Unmanned Air Vehicle (LADFUAV)

For each case, the configuration and computational grids are described, and CFD results in the form of pressure contour plots, velocity vectors and graphs are presented. CFD results are compared with corresponding experimental data.

A typical run on a good resolution grid (183 x 176) will approximately take 3 CPU hours on the Cray SV1ex machine (500 MHz clock speed which is equivalent to 2.0 GHz for a personal computer (PC) machine) at Ames Research Center. Specifically, it takes 2.17 CPU seconds for each iteration step and 5000 iterations for a complete calculation. The present code is based on a sequential algorithm and is not easily parallelized. Therefore, taking advantage of multiple processors is not possible. However, the code can be run on a PC machine. It takes 4.7 CPU hours to run the same calculation on a PC machine with a 750 MHz processor. The turn around time will improve for machines based on the latest Intel processors (3.06 GHz, or even faster clock speed).

Trek Aerospace's Ducted Fan

The first configuration chosen to validate the solver was Trek Aerospace's ducted fan, shown in Figure 8. This configuration consists of a duct, nacelle and fan. The duct has a diameter of 38.073 inches with a fan

Fig. 8 Trek Aerospace's ducted fan configuration

to duct tip clearance of 0.0367 inches. The fan has 5 blades with a tip diameter of 38 inches.

For this case, the flow solver was applied to the Trek Aerospace's ducted fan for seven different operating conditions in hover to construct the overall fan performance map. Both duct and nacelle were considered in the simulation while the fan was modeled by source terms in the momentum equations, as explained earlier.

The velocity profiles at three different fan speeds (2000, 3000 and 4000 RPM) are shown in Figure 9. In all cases, flow upstream and inside the duct are streamlined and reversed flow in the wake is observed downstream and outward from the duct. This reversed flow becomes stronger as the fan speed increases. Inside the duct, on the suction side near the fan tip, flow accelerates, and the velocity magnitude increases at higher RPMs.

Figure 10 depicts the pressure distribution around the duct and nacelle for the same operating conditions. The pressure increases as the flow passes through the fan as a consequence of the work on the fluid by the fan. Calculations reveal that the change in the pressure through the fan is higher near the fan tip region (see Figure 10), indicating that most of the pressure is created by the fan tip. In the wake region, high gradient pressure regions are observed at the same location where the reversed flow occurs. These high pressure regions are related to the vortex shedding and are stronger as the fan speed increases.

The torque and thrust were calculated from the load distribution on the blades using blade element theory. A comparison between the CFD-predicted ducted fan torque and wind tunnel measurements[21,22] at different fan speeds is shown in Figure 11. The computed

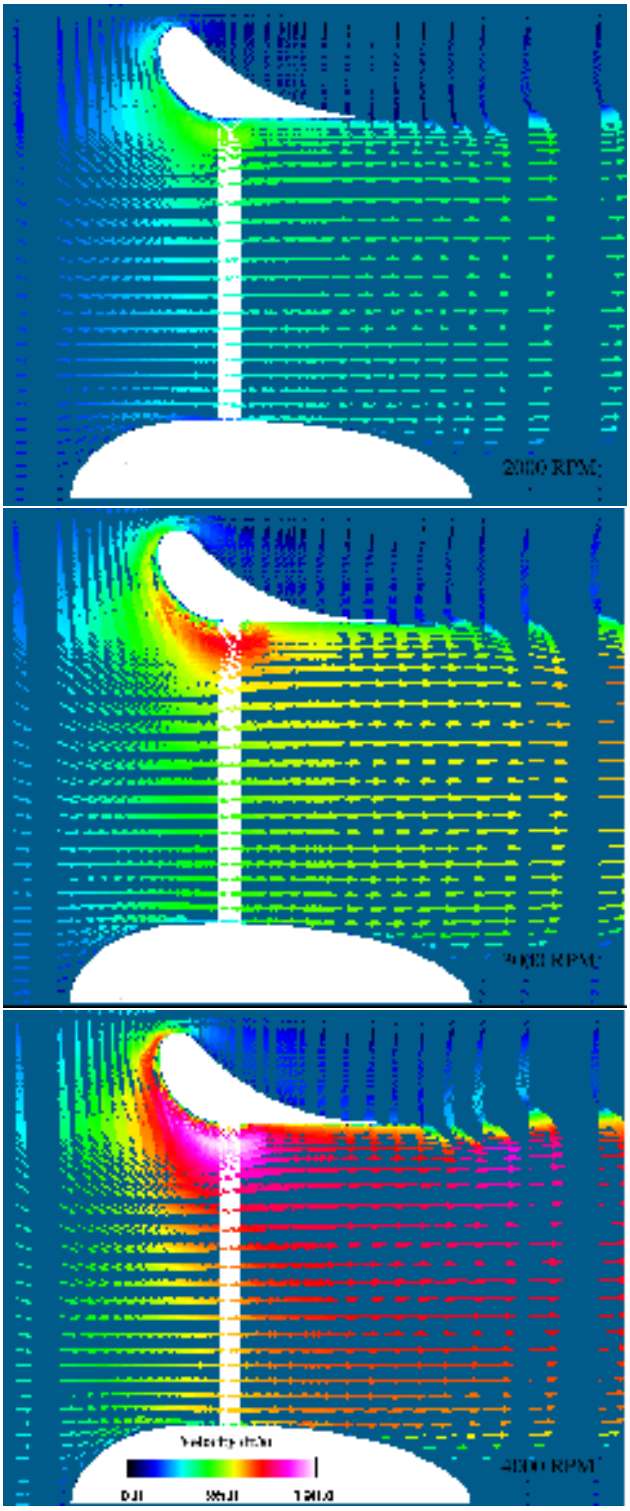

Fig. 9 Velocity vector plot around Trek Aerospace's fan at RPM=2000, 3000, 4000

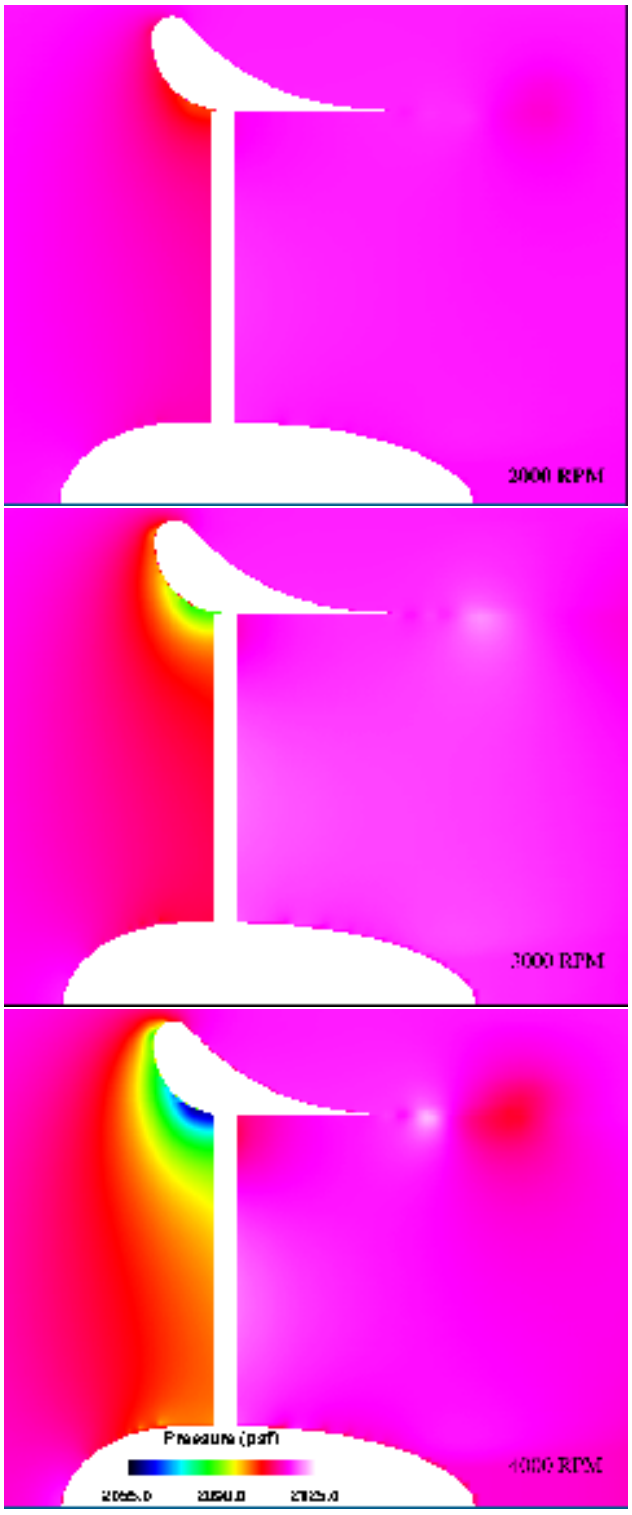

Fig. 10 Pressure distribution around Trek Aerospace's fan at RPM=2000, 3000, 4000

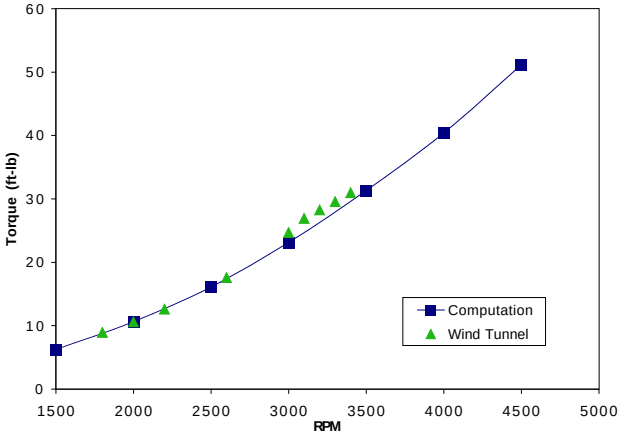

Fig. 11 Comparison of fan torque from CFD results and wind tunnel testing for Trek Aerospace's fan at different RPMs

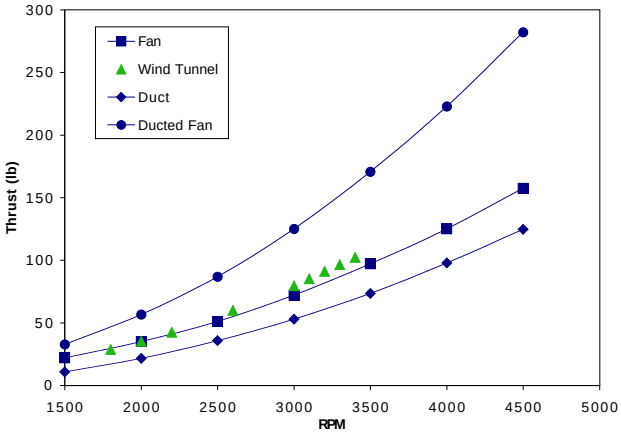

Fig. 12 Comparison of fan thrust from CFD results and wind tunnel testing for Trek Aerospace's fan at different RPMs

ducted fan torques are within 2 percent of the experimental data. The corresponding comparison of thrust is plotted in Figure 12. In computation, the thrust of a ducted fan consists of two parts, one for fan and the other for duct. The wind tunnel data is in closer agreement with the fan thrust rather than the total thrust distribution. This phenomenon could possibly be due to the disrupted flow in the lower quadrant of the test article, and the presence of support structures within the duct. After using *ad hoc* correction formula,[23] the wind tunnel hover values become:[21]

Thrust Coefficient = 0.213, Power Coefficient = 0.082, Figure of Merit = 0.7068.

The computed thrust coefficient, power coefficient, and figure of merit distributions are shown in Figure 13, respectively. Overall, the thrust coefficient is within 3 percent of the corrected test data; the power coefficient and the figure of merit, within 2 percent of those of corrected experimental data.

Increasing the blade pitch can increase thrust levels at the cost of higher power levels to turn the fan. A per-

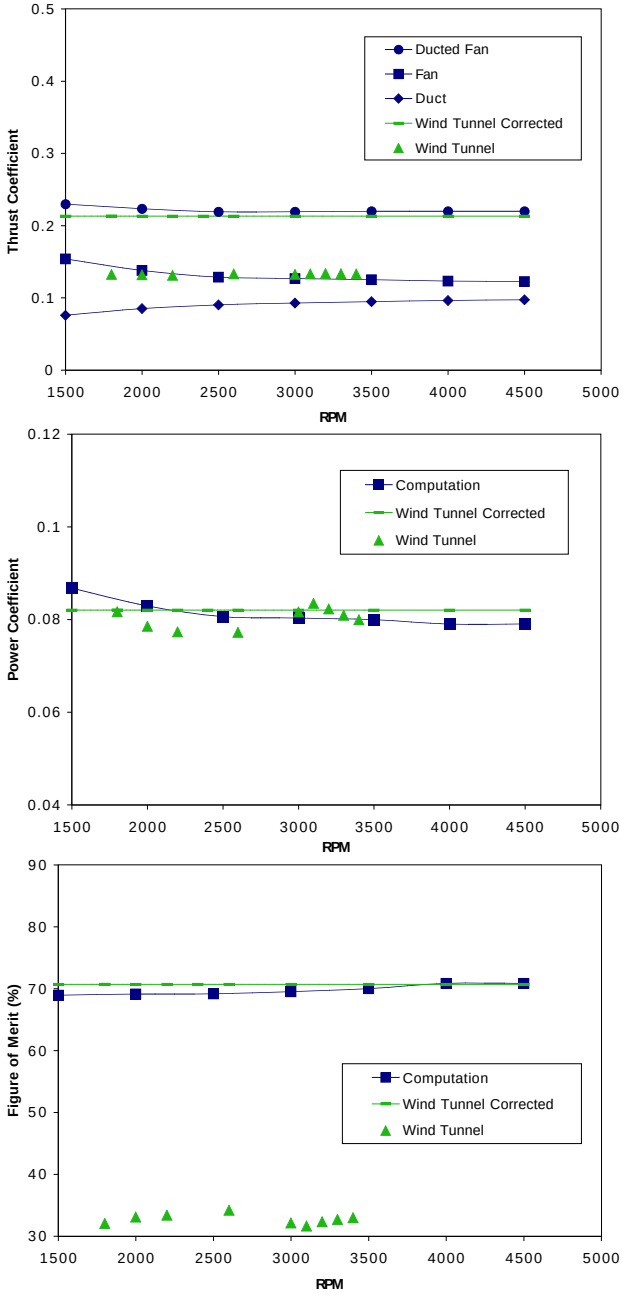

Fig. 13 Comparison of thrust, power, and figure of merit distributions from CFD results and wind tunnel testing for Trek Aerospace's fan at different RPMs

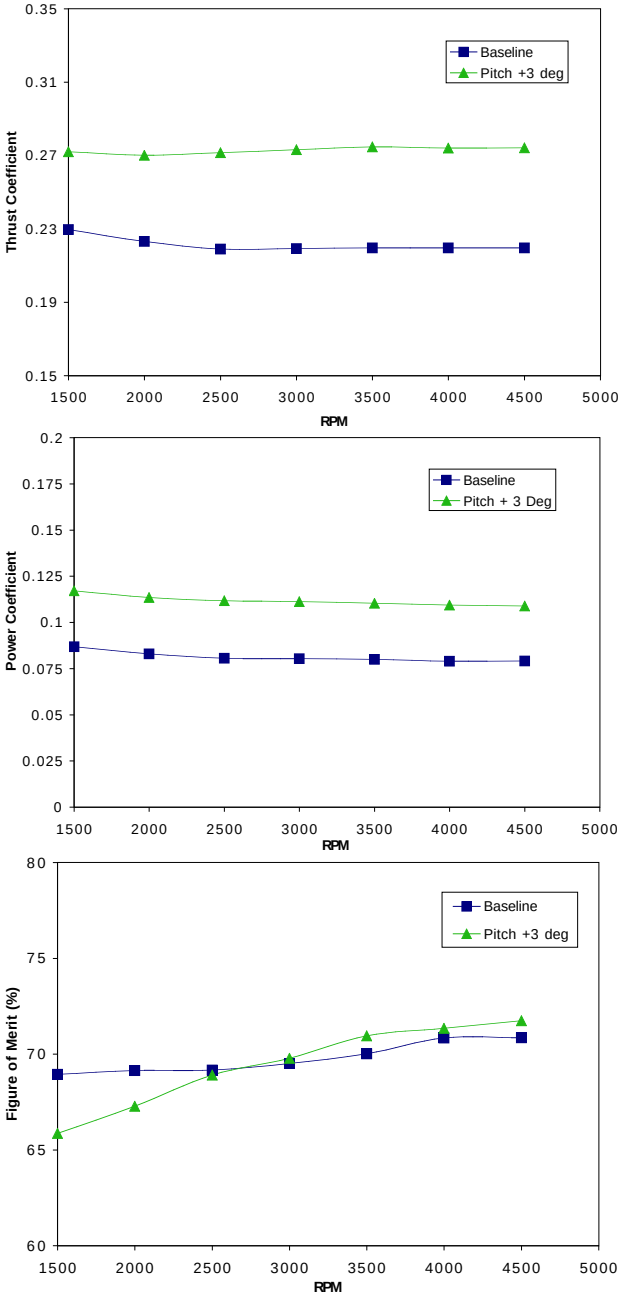

Fig. 14 Comparison of thrust, power, and figure of merit distributions of both the baseline fan and the fan with new pitch blades at different RPMs

formance comparison of the Trek Aerospace's ducted fan and a new ducted fan with blade pitch increased by 3 degrees is shown in Figure 14. At the 3500 RPM, the new ducted fan delivered 25 percent more thrust but required 37.5 percent more power. The figure of merit was only improved 1.43 percent at this RPM. Comparing with the baseline, the new ducted fan performed better for RPMs greater than 2700 but worse for RPMs less than 2700. The fan blade design enhancement is not simple. Even the final pitch setting warrants an optimization code.

Micro-Craft's LADFUAV

The Micro-Craft LADFUAV configuration has a duct with a diameter of 9.0 inches and a two-blade fan with a diameter of 8.985 inches. A simulation was carried out in hover at 16,000 RPM.

The velocity-vector plot of the flow going through the duct is presented in Figure 15. Due to viscous effects, a reversed flow occurs near the inner surface of the duct. Similar to the previous case, a recirculating region is also observed downstream of the duct. Figure 16 shows a close region near the fan tip. It can be seen that

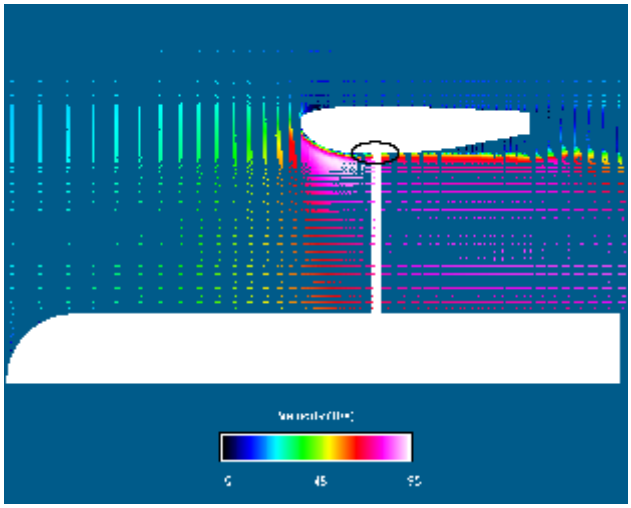

Fig. 15 Velocity distribution of Micro-Craft's LADFUAV in hover

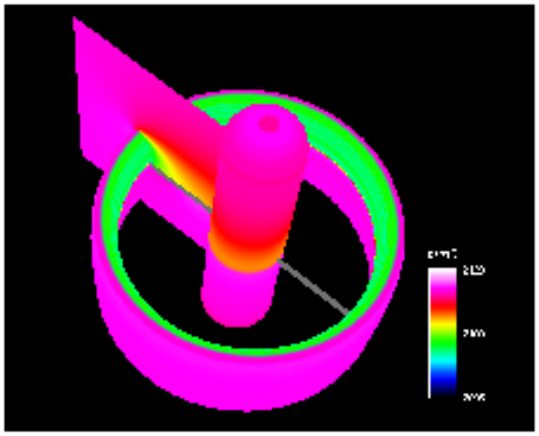

Fig. 17 Micro-Craft's LADFUAV duct pressure distribution

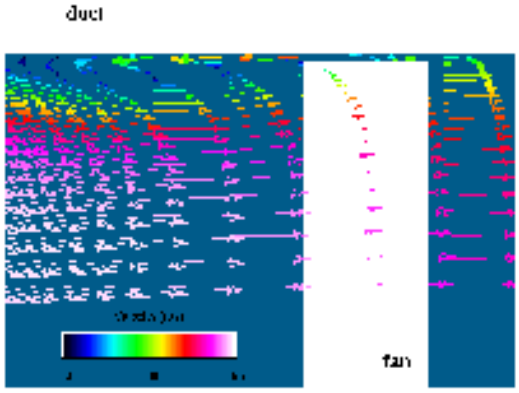

Fig. 16 Flow near the fan tip region of Micro-Craft's LADFUAV in hover

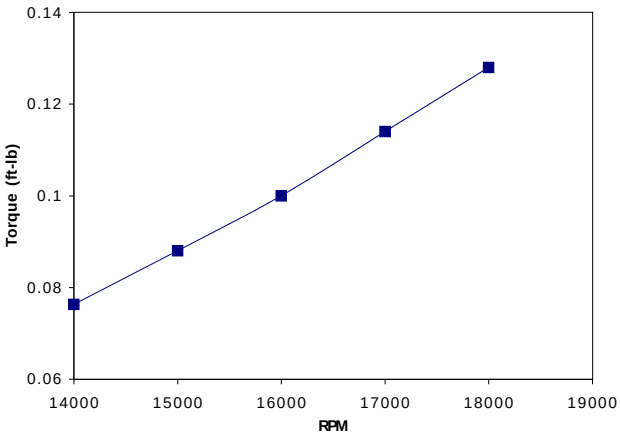

Fig. 18 Predicted fan torque of Micro-Craft's LADFUAV at different RPMs

recirculating flow occurs at the clearance between the duct and the fan.

Figure 17 depicts the pressure distribution on the duct with a section of the computational grid in the $r - z$ cutplane. The effect of the fan on the pressure distribution on the duct and nacelle is shown in this figure.

The torque and thrust were calculated from the load distribution on the blades using blade element theory. The predicted fan torque and thrust at different fan speeds are shown in Figure 18 and Figure 19, respectively. Further aerodynamic performance analysis was reported in Figure 20.

Conclusions

An axisymmetric Navier-Stokes flow code was developed to calculate the flow field of a ducted fan. Predictions of hover performance for two industrial ducted fan models of current interest were calculated. One of

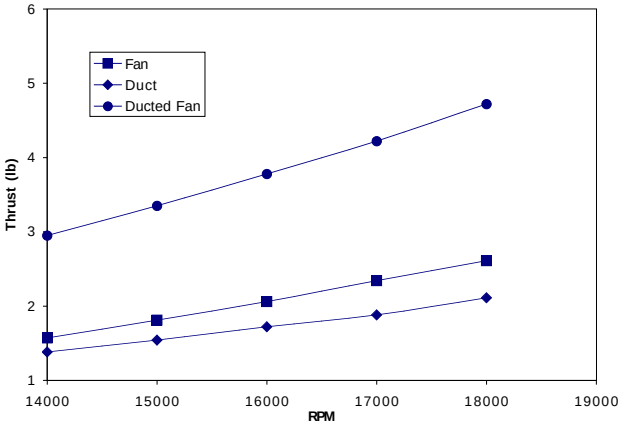

Fig. 19 Predicted fan thrust of Micro-Craft's LADFUAV at different RPMs

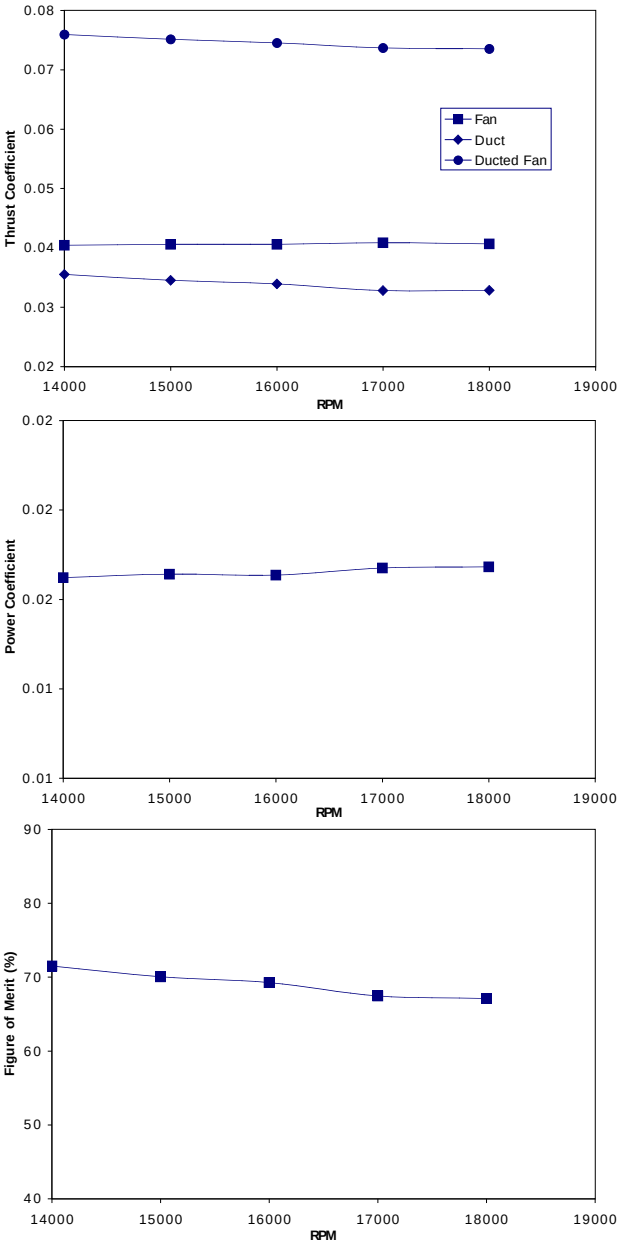

Fig. 20 Predicted thrust, power, and figure of merit distributions of Micro-Craft's LADFUAV at different RPMs

them was compared with available wind tunnel test data. The comparison was good. The thrust coefficient was within 3 percent of the corrected test data; the power coefficient and the figure of merit within 2 percent of those of the corrected wind tunnel data. Preliminary results showed that the present code is accurate and can be used as an axial flow analysis tool for ducted fan design.

The next step in code development for the ducted fans will consider three-dimensional hover flight conditions where the axisymmetric assumption will be removed to account for the fan blade azimuthal position. Further development of the research project will encompass unsteady axial and forward flight conditions with duct fan geometry including control panels and support structure within the duct.

Acknowledgements

The wind tunnel model of ducted fan was provided by Michael M. Moshier and Robert W. Bulaga of Trek Aerospace. The geometry of the Lift Augmented Ducted Fan Unmanned Air Vehicle was given by Larry Lipera of Micro Craft Inc.. Helpful discussions and suggestions were received from Anita Abrego, Frank Caradonna, Wayne Johnson, Roger Strawn, Chee Tung and William Warmbrodt. Their close cooperation to advance the ducted fan technology is gratefully acknowledged.

References

[1]B.W. McCormick. *Aerodynamics of V/STOL Flight*. Academic Press, New York, 1967.

[2]S. Thurston and R. C. Amsler. Review of marine propellers and ducted propeller propulsive devices. *Journal of Aircraft*, 3, May-June 1966.

[3]D. L. Kohlman. *Introduction to V/STOL Airplanes*. Iowa State University Press, Iowa, 1981.

[4]M. R. Mendenhall and S. B. Spangler. Theoretical study of ducted fan performance. *NASA CR-1494*, January 1970.

[5]M. R. Mendenhall and S. B. Spangler. Theoretical study of ducted fan performance. *NASA CR-1495*, January 1970.

[6]R. B. Gray and T. Wright. A vortex wake model for optimum heavily loaded ducted fans. *Journal of Aircraft*, 7, March-April 1970.

[7]P. F. Yaggy and K. W. Mort. A wind tunnel investigation of a 4–foot diameter ducted fan mounted on the tip of a semispan wing. *NASA TN D-776*, March 1961.

[8]P. F. Yaggy and K. W. Goodson. Aerodynamics of a tilting ducted fan configuration. *NASA TN D-785*, March 1961.

[9]K. J. Grunwald and K. W. Goodson. Aerodynamic loads on an isolated shrouded–propeller configuration for angles of attack from −10 deg to 110 deg. *NASA TN D-995*, January 1962.

[10]K. W. Mort. Performance characteristics of a 4–foot diameter ducted fan at zero angle of attack for several fan blade angles. *NASA TN D-3122*, December 1965.

[11]D. G. M. Davis. Ducted propulsors – Progress in the United Kingdom. *Business Aircraft Meeting, Wichita, Kansas, Society of Automative Engineers, Paper No. 750534*, 1975.

[12]K. W. Goodson and K. J. Grunwald. Aerodynamic characteristics of a powered semispan tilting-shrouded-propeller VTOL model in hovering and transition flight. *NASA TN D-981*, January 1962.

[13]K. W. Mort and P. F. Yaggy. Aerodynamic characteristics of a 4–foot diameter ducted fan mounted on the tip of a semispan wing. *NASA TN D-1335*, April 1962.

[14]Jr. Newsom, W. A. Aerodynamic characteristics of four–duct tandem VTOL–aircraft configurations. *NASA TN D-1481*, January 1963.

[15]E. E. Davenport and K. P. Spreemann. Transition characteristics of a VTOL aircraft powered by four ducted tandem propellers. *NASA TN D-2254*, April 1964.

[16]K. P. Spreemann. Wind tunnel investigation of longitudinal aerodynamic characteristics of a powered four–duct propeller VTOL model in transition. *NASA TN D-3192*, April 1966.

[17]Patankar S.V. *Numerical Heat Transfer and Fluid Flow*. Hemisphere Publishing Corporation, New York, 1980.

[18]Rajagopalan R.G. and Lim C.K. Laminar flow analysis of a rotor in hover. *Journal of the American Helicopter Society*, 36:12–23, 1991.

[19]Rajagopalan R.G. and Mathur S. Three dimensional analysis of a rotor in forward flight. *Journal of the American Helicopter Society*, 38:14–25, 1993.

[20]Rajagopalan R.G. and Zori L. Navier-Stokes calculations of rotor-airframe interaction in forward flight. *Journal of the American Helicopter Society*, 40:57–67, 1995.

[21]Moshier M. and Bulaga R. W. Wind tunnel performance investigation of the Solotrek XFV ducted fan system. *DARPA/DSO, Arlington, VA*, 2001.

[22]Abrego A. I. and Bulaga R. W. Performance study of a ducted fan system. *AHS Aerodynamics, Acoustics, and Test and Evaluation Technical Specialists Meeting, San Francisco, CA*, January 23-25, 2002.

[23]Mort K. W. Exit pressure data for a 38 inch diameter ducted fan in 7 x 10 ft wind tunnel. *DARPA/DSO, Arlington, VA*, 2001.